

See discussions, stats, and author profiles for this publication at: <https://www.researchgate.net/publication/51474129>

Diffusion-Photodynamics Coupling in Fluorescence Correlation Spectroscopy Studies of Photoswitchable Green Fluorescent Proteins: An Analytical and Simulative Study

ARTICLE *in* THE JOURNAL OF PHYSICAL CHEMISTRY B · AUGUST 2011

Impact Factor: 3.3 · DOI: 10.1021/jp205147n · Source: PubMed

CITATIONS

2

READS

29

5 AUTHORS, INCLUDING:



Niccolo Banterle

European Molecular Biology Laboratory

8 PUBLICATIONS 160 CITATIONS

SEE PROFILE



Laura D'Alfonso

Università degli Studi di Milano-Bicocca

57 PUBLICATIONS 716 CITATIONS

SEE PROFILE



Maddalena Collini

Università degli Studi di Milano-Bicocca

79 PUBLICATIONS 1,196 CITATIONS

SEE PROFILE



Giuseppe Chirico

Università degli Studi di Milano-Bicocca

140 PUBLICATIONS 2,079 CITATIONS

SEE PROFILE

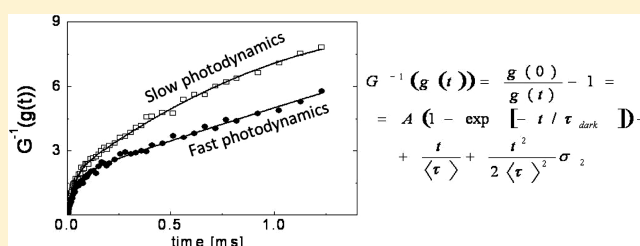
Diffusion–Photodynamics Coupling in Fluorescence Correlation Spectroscopy Studies of Photoswitchable Green Fluorescent Proteins: An Analytical and Simulative Study

S. C. Daglio, N. Banterle, L. D'Alfonso, M. Collini, and G. Chirico*

Dipartimento di Fisica, Università degli Studi di Milano Bicocca, Piazza della Scienza 3, I-20126, Milano, Italy

Supporting Information

ABSTRACT: The photodynamics of the Green Fluorescent Protein (GFP) has been addressed in detail, particularly by means of Fluorescence Correlation Spectroscopy (FCS), a technique that provides direct information when the diffusion and the photodynamics time scales are well separated. Efficient photoswitchable GFPs, a crucial component for applications in nanoscopy imaging, have long residence times in the dark state, typically longer than the diffusion time of the protein through the observation volume. In these cases, the effect of the coupling between photodynamics and the diffusion process on the analysis of the FCS measurements cannot be disregarded, and the use of FCS methods becomes therefore critical. This work deals with the analytical and simulative study of such coupling and indicates that the corrections to be applied to the conventional decoupled FCS model scale as the square root of the ratio between the diffusion and the dark state relaxation times. We discuss the possibility to estimate the extent of the diffusion/photodynamics coupling from the analysis of the inverse of the fluorescence autocorrelation function $g(t)$, defined as $G^{-1}(g(t)) = g(0)/g(t) - 1$. The function $G^{-1}(g(t))$ is analyzed in terms of a parabolic expansion in which the curvature term directly provides the desired measure of the coupling. We validate the analytical prediction and the graphical estimate of the coupling on simulations of FCS experiments that are based on a coupled Monte Carlo–Brownian Dynamics algorithm. The analysis of the curvature of $G^{-1}(g(t))$, applied to experimental FCS data of the photoswitchable E222Q mutant of GFPmut2 (Mut2Q), indicates that the trapping rate for this chromophore is 3 orders of magnitude underestimated when the diffusion/photodynamics coupling is not taken into account and sheds some additional light on the complex energy diagram for this protein.



INTRODUCTION

Fluorescence Correlation Spectroscopy (FCS) has been for more than two decades an extremely valuable tool for studying the diffusion and the photodynamics of chromophores coupled to fluorescence emission.^{1–6} This is documented by various reviews^{7–11} and by papers on organic chromophores^{12–15} and on intrinsically fluorescent proteins;^{4,5,16–21} moreover, a number of experimental and theoretical improvements of FCS are being continuously reported.^{22–25}

We can obtain direct information on the molecular photodynamics when the diffusion relaxation time, $\tau_{\text{diff}}^{(xy)}$, is sensibly larger than the characteristic times of the transitions between states. Depending on the excitation mode, either one- (OPE) or two-photon excitation (TPE), the characteristic diffusion relaxation time depends on the laser beam waist, ω_{xy} , and on the molecule diffusion coefficient, D_T , as: $\tau_{\text{diff}}^{(xy)} = \omega_{xy}^2/(\nu D_T)$, with $\nu_{\text{OPE}} = 4$ and $\nu_{\text{TPE}} = 8$. For Green Fluorescent Proteins (GFPs), typically composed of 238 aa and 27 kD in weight, the molecular size is of the order of 2 nm, and the diffusion coefficient is about $100 \mu\text{m}^2/\text{s}$. The diffusion time of the protein through a beam waist $\omega_{xy} = 0.5 \mu\text{m}$ is about 1 ms. Hundreds of microseconds photodynamics, or faster, can then be studied by means of FCS experiments and singled out in the AutoCorrelation Functions (ACFs).

Optical nanoscopy strives for the development of dedicated photochromic molecules.²⁶ The basic requirement for nanoscopy application²⁷ is a nonuniform excitation pattern and the presence of an excited bright state, B, that can be photoconverted to an excited dark state, D. Contrary to the $D \rightarrow B$ transition, the rate of the $B \rightarrow D$ transition depends on the light intensity times the excitation cross-section, σ . The spatially confined inhibition of the fluorescence emission in a selected spectral band depends critically on the excitation intensity and on the relaxation rate between the dark and the bright states, k_{DB} . The possibility to shape the Point Spread Function (PSF) by stimulated emission of the molecules at the boundaries of the PSF diminishes in fact at intensity values larger than the saturation intensity, $I_{\text{sat}} = k_{\text{DB}}/\sigma$. Therefore, the longer the residence time of the dark state, the smaller the saturation intensity is and the lower the intensity required to inhibit the fluorescence emission on the edges of the PSF of the microscope. It can then be understood why long-lived dark photoswitchable states are searched among the wide class of fluorescent proteins and their mutants.

Received: January 13, 2011

Revised: July 5, 2011

Published: July 07, 2011

The study of the photodynamics of such slowly relaxing photoswitchable proteins could in principle be done by FCS only after taking proper account of the coupling between the diffusion and the photoactivation dynamics. Approximated FCS approaches to the photodynamics of long-lived states in GFPs has been proposed in the past,^{4,6} using the simplifying assumption in which the diffusion and the photodynamics time scales are decoupled. These approaches have also exploited the fluorescence enhancement that is induced by photoswitching.⁶

We present here an analytical and simulative study of the effect of the coupling between the diffusion and the photoactivated fluorescence fluctuations on the ACF, $g(t)$. The analytical study, also compared to the results of Monte Carlo–Brownian Dynamics simulations, indicates that the effect on the retrieved fraction of dark molecules scales as the square root of the ratio between the diffusion and the dark state relaxation times. We develop a graphical analysis of the ACF to estimate the amount of coupling starting from the evaluation of the long lag time curvature of the inverse of the ACF, $G^{-1}(g(t)) = g(0)/g(t) - 1$. The numerical simulations and the graphical analysis of the ACFs, performed by means of the $G^{-1}(g(t))$ function, are also applied to experimental data on the photoswitchable GFPmut2 E222Q mutant (Mut2Q).⁶

METHODS

Molecular Diffusion and Photodynamics Algorithm.

The system that we simulate is a dilute solution of globular proteins, carrying a chromophore with a complex photodynamics, characterized by at least two excited states with different brightness values. The brightest excited state has a lifetime in the nanosecond time scale, while the photoactivation process, related to the population/depletion of the dark state, may occur on a wide time range, 1–10 000 μ s. The energy diagrams of the fluorescent proteins may be very complex^{4,6,28,29} as sketched, for example, in Figure 1A and B. A pump laser beam primes the $S_0 \rightarrow S_1$ transition of the bright state that may convert to a trap/dark state D or a triplet state T. A second laser beam, called “probe” beam, causes the transition from the trap state D to a higher-energy state, D^* (see Figure 1). The subsequent recovery of the S_0 state occurs either through a transition to S_1 (adiabatic transition, Figure 1A) or directly to S_0 (diabatic transition, Figure 1B). Through both the paths we obtain the depletion of the trap/dark state D. Additionally, transitions to higher-energy states (S_n) are allowed. We refer to the caption of Figure 1 for the definition of the photodynamics parameters.

We can simplify the energy diagrams reported in Figure 1A, B to the schemes 1C and 1D by assuming that the relaxation of the D^* state is very rapid ($\gamma_2 \gg k_{32}$). In this case, the pump laser beam primes the transition from S_0 to S_1 , and the probe beam induces transitions directly from the long-lived state D. Photo-switching is modeled by assuming either that the $S_1 \rightarrow D$ transition rate, k_{23} , is reduced (scheme 1C) or the $D \rightarrow S_0$ transition rate is increased (scheme 1D) by the term $\sigma_{32}I_{\text{probe}}$.

We outline here the mixed Brownian dynamics—Monte Carlo algorithm for the simulation of the fluorescence ACFs. Additional details and testing of the algorithm can be found in the Supporting Information (SI: “Simulation Algorithm”). To simulate the output of the FCS experiment, we must take into account three steps: the simulation of the molecular Brownian diffusion and of the photodynamics of the particular chromophore, possibly coupled to the diffusion, and the calculation of the ACF of

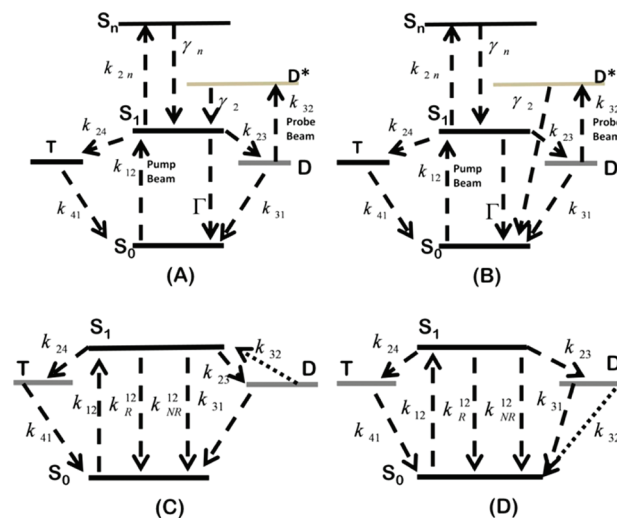


Figure 1. Examples of two energy diagrams that may describe part of the complex photodynamics in FPs. S_0 , S_1 , and S_n are the ground, the first, and the n th excited singlet states. The $S_0 \rightarrow S_1$ transition is primed by a first laser, called pump laser. T is a triplet state, and D is a dark state, not necessarily a triplet state, but endowed with a much lower brightness than S_1 . The rates k_{23} and k_{31} refer to the population (from S_1) and the spontaneous depopulation (to S_0) of the dark state D. The rates k_{24} and k_{41} refer to the population (from S_1) and depopulation (to S_0) of the triplet state T. The two schemes differ for the effect of the second laser beam, called probe laser, that pumps the molecules from the trap state onto a higher-energy one, D^* , from which the chromophore decays either adiabatically to S_0 , through S_1 and possibly a photon emission (panel A) or diabatically to S_0 (panel B). The excitation rates of the chromophore under the pump (k_{12}) and probe (k_{32}) beams are related to the corresponding intensities cross sections, σ_{12} and σ_{32} , by $k_{12} = \sigma_{12}I_{\text{pump}}$ and $k_{32} = \sigma_{32}I_{\text{probe}}$. Panels C and D report the simplified versions (for $\gamma_2 \gg k_{32}$) of the energy diagrams that are used for the analytical development: k_{12}^{R} and k_{12}^{NR} are the radiative and nonradiative relaxation rates from the first excited state ($\Gamma = k_{12}^{\text{R}} + k_{12}^{\text{NR}}$).

the fluorescence fluctuations. For this reason, the simulation model implemented in the code is organized on three different time scales:³⁰

- $dt \cong 20\text{--}200$ ns is associated to the Brownian Diffusion (BD) process;
- $dT = 20$ ns characterizes the photodynamics (PD);
- $\tau = 200$ ns represents the minimum lag delay in the ACF computation.

The Brownian dynamic propagator, implemented according to refs 31 and 32 operates every time-step whose duration is dt , and the photodynamics algorithm is implemented every dT/dt steps. The ACF calculation is called at the end of the whole simulation with a lag time that is a multiple of τ .

All the simulations were run on the Lagrange Computation Server at Interuniversity Consortium for the Numerical Computation (Cilea, www.cilea.it). The simulation code has been implemented in a single C thread. The code is organized on three levels of subroutines. The proteins are simulated as single spheres whose motion satisfies the Langevin equation.³³ As detailed in the SI (“Simulation Algorithm”), we have checked that the choice of the BD time step ensures that for molecules of the size of GFP the Stochastic Dynamics algorithm can be applied.³³ The choice of the PD time scale, $dT = 20$ ns, much longer than the singlet excited state lifetime, ensures that in each PD step the molecule,

if in an excited state, decays to the ground state through one of the possible routes reported in the scheme of Figure 1.

Of the three steps of the simulation algorithm, we describe here in detail the photodynamics Monte Carlo algorithm only and leave the description of the BD algorithm and the ACF computation to the SI (“Simulation Algorithm”) since they are standard procedures.

Photodynamics. Each protein diffusing in the simulation box is endowed with an integer variable, the Optical Label (OL) flag, that codes for its photodynamic state. At the beginning of the simulation, all the OLs are initialized to zero, indicating that all the molecules start their PD history in S_0 . At each PD time step dT , a Monte Carlo (MC) test is performed, and the OL flag switches to values that characterize the states S_1 (OL = 1), T (OL = 2), and D (OL = 3). The transition probability is chosen according to a standard MC test that allows us to simulate the PD on a single chromophore and implement it within the Langevin formalism adopted to solve the diffusion motion. Alternative approaches that work within the Smoluchowski framework³³ follow the well-known Gillespie algorithm for the simulation of stochastic chemical reactions.³⁴

If the OL flag is 0, a MC test is performed on the $S_0 \rightarrow S_1$ transition. To minimize the CPU time (as discussed in the SI, “Effect of the beam shape on the simulated ACF”), it is computationally convenient to adopt a two-photon excitation (TPE) mode with spatial dependence of the excitation probability given by

$$k_{12}^{(TPE, G3D)} = k_{12} [\rho_{G3D}(x, y, z)]^2$$

$$\rho_{G3D}(x, y, z) = \frac{1}{\pi^{1.5} \omega_{xy}^2 \omega_z} \exp \left[-2 \frac{(x^2 + y^2)}{\omega_{xy}^2} - 2 \frac{z^2}{\omega_z^2} \right] \quad (1)$$

The excitation rate is computed as $k_{12} = \sigma_{TPE} I_{\text{pump}}^2$. For the probe beam excitation, a similar algorithm is assumed with $k_{32} = \sigma_{32} I_{\text{probe}}$. Other excitation modes are discussed in the SI (“Effect of the beam shape on the simulated ACF”) and do not imply substantial changes in the discussion of the Results. The parameters ω_{xy} and ω_z depend on the objective numerical aperture and the laser wavelength. The values of these parameters are chosen according to the experimental conditions to be simulated (see also the “Effect of the beam shape on the simulated ACF” section in the SI). The chromophore excitation probability for the $S_0 \rightarrow S_1$ transition is $P_{12} = k_{12} dT$, and the transition is accepted if $\xi_1 \leq P_{12}$, where ξ_1 is a uniform random number. In this case, the OL flag is switched to 1.

When the chromophore is on the S_1 state (OL = 1), a second Monte Carlo test, acting on the same PD simulation step, chooses which of the following de-excitation pathways the protein undertakes.

Radiative and Nonradiative Relaxation to S_0 . In this case, the OL flag is reset to 0. The total $S_1 \rightarrow S_0$ de-excitation rate, Γ , in Figure 1 is given by the sum of the radiative, k_{12}^R , and nonradiative, k_{12}^{NR} , decay rates. When the radiative pathway is sampled, the emitted photon adds into the Fluorescence Time Vector (FTV) counter that provides the fluorescence time trace used for the ACF computation.

Intersystem Crossing to T or Conversion to D. In these cases, the OL flag switches to 2 and 3, respectively. The rates k_{23} and k_{24} refer to the $S_1 \rightarrow T$ and the $S_1 \rightarrow D$ transition, respectively, and $k_{\text{tot}} = \Gamma + k_{23} + k_{24}$. The T state is a triplet state from which the molecule relaxes to S_0 , mainly through nonradiative processes. These relaxation modes produce exponential components in the

ACF decays with characteristic times of the order of a few microseconds.^{5,16} The D state is the dark state involved in the photo-switching. It may correspond to a modified chemical structure, and it is typically not a triplet state.³⁵

If ξ_2 is a uniformly distributed random number, the test can be summarized as follows

$$\begin{aligned} \text{if } \xi_2 \in [0; k_{12}^R/k_{\text{tot}}] & : S_1 \rightarrow S_0 \text{ radiative} \\ \text{if } \xi_2 \in (k_{12}^R/k_{\text{tot}}; (k_{12}^R + k_{12}^{NR})/k_{\text{tot}}] & : S_1 \rightarrow S_0 \text{ nonradiative} \\ \text{if } \xi_2 \in ((k_{12}^R + k_{12}^{NR})/k_{\text{tot}}; (k_{12}^R + k_{12}^{NR} + k_{23})/k_{\text{tot}}] & : S_1 \rightarrow T \\ \text{if } \xi_2 \in ((k_{12}^R + k_{12}^{NR} + k_{23})/k_{\text{tot}}; 1] & : S_1 \rightarrow D \end{aligned} \quad (2)$$

We finally need to consider the decay paths from T and D according to

$$\begin{aligned} \text{if } \{ \text{OL} = 2 \text{ and } \xi_3 \in [0; dT k_{31}] \} & : T \rightarrow S_0 \text{ and OL} = 0 \\ \text{if } \{ \text{OL} = 3 \text{ and } \xi_3 \in [0; dT k_{41}] \} & : D \rightarrow S_0 \text{ and OL} = 0 \end{aligned} \quad (3)$$

where ξ_3 is a third independent uniformly distributed random number in $[0, 1]$.

So far we have considered only the effect of the pump laser beam. Since we want to simulate photoswitching induced by a second beam (with intensity I_{probe}), we need to consider additional paths activated by the probe beam. When OL = 3, a fourth MC test is performed depending on the probe laser intensity. For the scheme 1C, the probability that the second beam stimulates the $D \rightarrow S_1$ transition is computed as $P_{32} = \sigma_{32} I_{\text{probe}} dT$ and compared to a fourth uniformly distributed random number, ξ_4 . If $P_{32} \leq \xi_4$, the protein OL flag is reset to 1, meaning that in the next photodynamic step the molecule may emit a photon with a probability k_{12}^R/k_{tot} . For the scheme 1D, instead, the probability P_{32} is used to ascertain whether the molecule undergoes a $D \rightarrow S_0$ transition, and OL is set to 0: in this case, no photon emission may occur, and the transition is diabatic. Both algorithms allow us to simulate the photoswitching of the chromophore and the related fluorescence enhancement (see SI for details).

Since the starting configuration corresponds to all molecules in the ground state, the electronic states of the molecules must first reach a dynamical equilibrium. This can be obtained by running 2 s of simulation: after this equilibration time, the simulations were run for approximately 80 s.

For the simulations of the fluorescence ACFs under dual (pump and probe) beam excitation and with a square modulation of the probe beam (at frequency ν_L), we evaluate for every time step t the factor $N = t\nu_L$ and set $I_{\text{probe}} = 0$ only if $N - \text{round}(N) < 0.5$.

The mixed BD–MC algorithm was first extensively tested for reproducing the known analytical shape and amplitude of the fluorescence fluctuation ACF. For the case of fluorescence fluctuations induced only by diffusion (reported in the SI, “Numerical Simulation Analysis of the short-lived dark state photodynamics” and “Effect of the beam shape on the simulated ACF”), the simulations indicate that by choosing the TPE excitation mode with a 3D Gaussian beam shape (eq 1) and the simulation box volume $\cong 135 \mu\text{m}^3$ we can correctly reproduce the ACF decay, and an analytical fitting function for the fluorescence ACF can be used (as reported below in eq 4). The more realistic Gaussian–Lorentzian shape, on the contrary, would imply a nonanalytical fitting function and the use of a much larger simulation box due to the slow axial decay of the Lorentzian

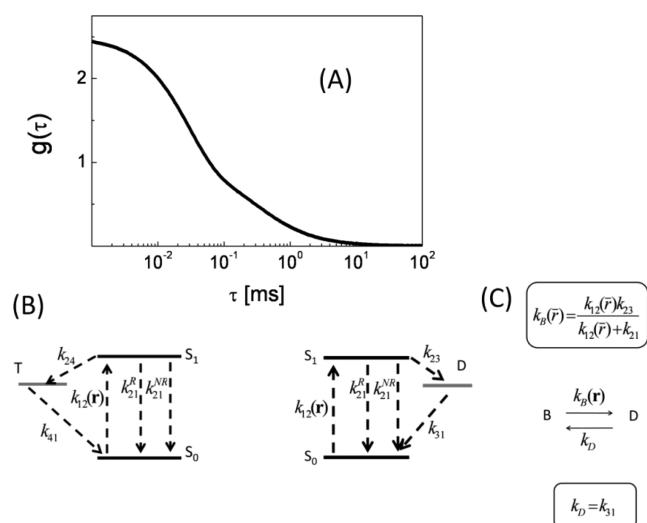


Figure 2. Typical short-lived triplet state ACF predicted from eq 4, $\tau_{\text{diff}}^{(xy)} = 300 \mu\text{s}$, $\tau_{\text{diff}}^{(z)} = 3000 \mu\text{s}$, $f_{\text{dark}} = 0.6$, and $\tau_{\text{dark}} = 30 \mu\text{s}$. Panel B: three-state (S_0 – S_1 – T) energy diagram scheme that describes the flickering of the fluorescence emission from a single fluorophore. The T state is a triplet short-lived dark state. The rate k_{24} is the intersystem crossing rate. Panel C: three-state (S_0 – S_1 – D) energy diagram scheme that describes the trapping of the excited state chromophore in a dark long-lived state D . The bright state, S_1 , is resonant with the radiation and is coupled to a dark state, D . The rates between the states are: the position-dependent excitation rate, $k_{12}^R(\bar{r})$, the radiative k_{21}^R and the nonradiative k_{21}^{NR} de-excitation rates, the $S_1 \rightarrow D$ crossing rate, k_{23} , and the de-excitation rate, k_{31} . We sketch also a simplified unimolecular reaction between two states, B (bright) and D (dark), that is equivalent to the three-state model. The equivalent forward and backward reaction rates $k_B(\bar{r})$ and k_D are defined in the text.

Table 1. Rate Constants for the E222Q Mutant of GFP from References 4 and 36^a

k_{24}	0.02 MHz
k_{41}	0.013 MHz
k_{21}^{rad}	400 MHz
k_{21}^{nonrad}	343 MHz

^a In the simulation, we have also assumed $\sigma_{\text{TPE}} = 3 \times 10^{-49} \text{ cm}^4 \cdot \text{s}$, $\omega_{xy} = 0.66 \mu\text{m}$, and $\omega_z = 1.55 \mu\text{m}$.

component of the beam shape. No substantial change in the main results of simulations discussed hereafter is expected for a different excitation mode and laser beam profile.

The simulation input rates for the basic three states (S_0 – S_1 – T) model (see Figure 2B) are chosen according to the values reported in the literature^{4,36} for the E222Q GFP mutant and reported in Table 1. The TPE cross-section is assumed here as $\sigma_{\text{TPE}} = 3 \times 10^{-49} \text{ s} \cdot \text{cm}^4$, in agreement with reported literature values for GFP mutants,^{37,38} and the beam waist sizes are $\omega_{xy} = 0.66 \mu\text{m}$ and $\omega_z = 1.55 \mu\text{m}$, similar to the experimental values in the experiments by Quercioli et al.⁶ The values of additional rates for a more complex energy diagram will be specified when needed in the text.

The algorithm just described can be generalized to include the effect of photobleaching. In this case, the photodynamic equations cannot be easily solved due to the lack of the conservation of the number of fluorescent molecules.³⁹ Moreover, photobleaching

was found to depend on the second, third, or even higher powers of the excitation intensity, depending on the fluorophore and the excitation mode, and it is mediated via higher singlet or triplet states, leading to the creation of reactive species, as shown by experiments performed with the addition of radical quenchers.^{14,40} Photobleaching could then be modeled in our Monte Carlo approach as a first-order rate from a higher-energy triplet state^{40,41} T_n since the high polarity of their molecular orbitals is typically responsible for the excited state chemical reaction that leads to photobleaching. Semianalytical models and experimental studies of the effect of photobleaching on the ACFs under one or two photon excitation have been presented in the literature,^{14,25,39–41} and we are not pursuing this study here.

RESULTS AND DISCUSSION

The report is organized as follows: the case of coupling between diffusion and photodynamics fluctuations is treated analytically for the simplified case of spherical excitation volume, and a simple scaling law is obtained. To verify the analytical results, we discuss a graphical analysis of the ACFs that allows us to estimate the amount of diffusion/photodynamics coupling. Finally, we validate both the simulation outputs and the graphical analysis of the ACFs on experimental data on the photoswitchable protein Mut2Q taken from the recent work by Quercioli et al.⁶

Mathematical Model of the Diffusion: Photodynamics Coupling. We focus here on the simple energy diagram given in Figure 2 and write a simple analytical form of the dark state fraction even for long-lived dark states. We use here the notation D , as “dark”, for long-lived trap states (Figure 2C) which may not necessarily be triplet states, and T , as “triplet”, for short-lived dim states, typically with triplet spin configuration.

Diffusion–Photodynamics Coupling: Analytical Result for a Short-Lived Dark State. The bright state can be found in the ground, S_0 , and in the excited electronic configuration, S_1 . When the bright–dark state kinetics falls in a frequency range that is higher than the diffusion rates, we can decouple the photodynamics (due to the $S \rightarrow T$ transition) and the diffusion process in the computation of the ACF of the fluorescence fluctuations (δF), which is the natural output of the FCS experiments according to⁸

$$g(t) = \frac{\langle \delta F(t+t_0) \delta F(t_0) \rangle_{t_0}}{\langle F(t) \rangle_{t_0}^2} = g_0 \left(1 + \frac{\tau}{\tau_{\text{diff}}^{(xy)}} \right)^{-1} \left(1 + \frac{\tau}{\tau_{\text{diff}}^{(z)}} \right)^{-0.5} \left[1 + \left(\frac{F_{\text{dark}}}{1 - F_{\text{dark}}} \right) \exp(-t/\tau_{\text{dark}}) \right] = g_{\text{diff}}(t) g_{\text{PD}}(t) \quad (4)$$

where $\tau_{\text{diff}}^{(xy)}$ is the diffusion time in the focal plane and $\tau_{\text{diff}}^{(z)} = \omega_z^2/(8D_T)$ is that along the optical axis. The extrapolation to zero lag time of the diffusive component of the ACF is g_0 , which is related to the average number of molecules in the excitation volume, $\langle N \rangle$, as $g_0 = \gamma/\langle N \rangle$ ($\gamma_{\text{OPE}} = 0.35$; $\gamma_{\text{TPE}} = 0.076$). The bright to dark kinetics parameters are the relaxation time τ_{dark} and the dark fraction D . eq 4 is valid only when $\tau_{\text{dark}} \ll \tau_{\text{diff}}^{(xy)} < \tau_{\text{diff}}^{(z)}$: in this case, the excitation intensity seen by the chromophore during its photodynamic cycle is substantially constant. If we assume that the excitation rate has no spatial dependence,

i.e., $k_{12}^{(\text{TPE,G3D})}(x,y,z) = k_{12}$, the relaxation time and the dark fraction are written as (see Figure 2B)

$$\begin{aligned}\tau_{\text{dark}} &= \frac{k_{12} + k_{21}}{k_{12}(k_{24} + k_{41}) + k_{21}k_{41}} \\ f_{\text{dark}} &= \frac{k_{12}k_{24}}{k_{12}(k_{24} + k_{41}) + k_{21}k_{41}}\end{aligned}\quad (5)$$

A more realistic model discussed in the literature^{23,42} suggests to average τ_{dark} and f_{dark} (eq 5) over the light intensity distribution ($\rho_{\text{G3D}}(x,y,z)$ in eq 1) to evaluate effective values of the photophysical parameters, $\tau_{\text{dark}}^{\text{eff}}$ and $f_{\text{dark}}^{\text{eff}}$

$$g_{\text{PD}}(t) = \left(\frac{f_{\text{dark}}^{\text{eff}}}{1 - f_{\text{dark}}^{\text{eff}}} \right) \exp \left[-\frac{t}{\tau_{\text{dark}}^{\text{eff}}} \right] + 1 \quad (6)$$

$$f_{\text{dark}}^{\text{eff}} = \frac{\int \frac{f_{\text{dark}}(\vec{r})}{1 - f_{\text{dark}}(\vec{r})} \rho_{\text{G3D}}^4(\vec{r}) dV}{\int \frac{\rho_{\text{G3D}}^4(\vec{r})}{1 - f_{\text{dark}}(\vec{r})} dV} \quad (7)$$

and

$$\tau_{\text{dark}}^{\text{eff}} = \frac{\int \frac{f_{\text{dark}}(\vec{r})}{1 - f_{\text{dark}}(\vec{r})} \rho_{\text{G3D}}^4(\vec{r}) \tau_{\text{dark}}(\vec{r}) dV}{\int \frac{\rho_{\text{G3D}}^4(\vec{r})}{1 - f_{\text{dark}}(\vec{r})} dV} \quad (8)$$

In eqs 7 and 8, the spatial dependence of τ_{dark} and f_{dark} is through the function $\rho_{\text{G3D}}(\vec{r})$ (eq 1). The numerical algorithm outlined in the Methods section allows us to recover the effects described by eqs 6–8 on the ACF in agreement with previous studies⁴² (see SI “Numerical Simulation Analysis of the short lived dark state photodynamics”). However, when the dark state is long-lived with respect to the diffusion time, even eqs 6–8 cannot describe correctly the experimental data. Additional and more important corrections to eq 4 must then be searched by solving the photodynamics and diffusion equations without the factorization of these two sources of fluctuations that led instead to eq 4. In the next paragraph, we describe a simple model that underlines the significant variables that must be taken into account when dealing with long-lived dark states.

Steady State Long-Lived Dark State Population. We want to derive a closed expression for the dark state population for a simple three-state model (see model in Figure 2C) from the solution of the coupled diffusion/photodynamics equations

$$\begin{aligned}\frac{\partial}{\partial t} c_{\text{S}_0}(\vec{r}, t) &= D_T \nabla^2 c_{\text{S}_0}(\vec{r}, t) - k_{12}(\vec{r}, t) c_{\text{S}_0}(\vec{r}, t) + k_{21} c_{\text{S}_1}(\vec{r}, t) + k_{31} c_{\text{D}}(\vec{r}, t) \\ \frac{\partial}{\partial t} c_{\text{S}_1}(\vec{r}, t) &= D_T \nabla^2 c_{\text{S}_1}(\vec{r}, t) + k_{12}(\vec{r}, t) c_{\text{S}_0}(\vec{r}, t) - (k_{21} + k_{23}) c_{\text{S}_1}(\vec{r}, t) \\ C &= c_{\text{S}_0}(\vec{r}, t) + c_{\text{S}_1}(\vec{r}, t) + c_{\text{D}}(\vec{r}, t)\end{aligned}\quad (9)$$

In these equations, we have assumed that the total protein concentration, C , is conserved (no photobleaching), and we have dropped the suffices “TPE, G3D” from the notation of the excitation rate $k_{12}(r)$. These equations can be approximated (see SI “Derivation of eq 10”) to a unimolecular chemical kinetics (see Figure 2B) in which the state B is the bright state, including both the ground (S_0) and excited (S_1) state

($B = \text{S}_0 + \text{S}_1$), and the D state is the dark state. The equations for diffusion and photodynamics of the “B” and “D” species are then

$$\begin{aligned}\frac{\partial}{\partial t} c_{\text{B}}(\vec{r}, t) &= D_T \nabla^2 c_{\text{B}}(\vec{r}, t) + k_{\text{D}} c_{\text{D}}(\vec{r}, t) - k_{\text{B}}(\vec{r}) c_{\text{B}}(\vec{r}, t) \\ \frac{\partial}{\partial t} c_{\text{D}}(\vec{r}, t) &= D_T \nabla^2 c_{\text{D}}(\vec{r}, t) - k_{\text{D}} c_{\text{D}}(\vec{r}, t) + k_{\text{B}}(\vec{r}) c_{\text{B}}(\vec{r}, t)\end{aligned}\quad (10)$$

In this equation, $k_{\text{B}}(\vec{r})$ indicates the rate constant related to the probability to enter the dark state (or to leave the bright one), and k_{D} is related to the transition from the dark state to the bright state. It must be noted that $k_{\text{B}}(\vec{r})$ is not the $k_{12}(\vec{r})$ rate reported in the energy diagram of Figure 2C since $k_{\text{B}}(\vec{r})$ refers to the rate at which the whole bright state B is depopulated and must then be proportional to the population of S_1 that depends on the singlet lifetime and the irradiating beam intensity. As derived in the Supporting Information, the expected functional form is $k_{\text{B}}(\vec{r}) = (k_{12}(\vec{r})k_{23})/(k_{12}(\vec{r}) + k_{21})$.

An estimate of the average dark state fraction in the presence of coupling between the diffusion and the photodynamics can be obtained from the equilibrium solution of eq 10

$$D_T \nabla^2 \langle c_{\text{D}}(\vec{r}) \rangle - k_{\text{D}} \langle c_{\text{D}}(\vec{r}) \rangle + k_{\text{B}}(\vec{r}) (C - \langle c_{\text{D}}(\vec{r}) \rangle) = 0 \quad (11)$$

$$\langle c_{\text{B}}(\vec{r}) \rangle = C - \langle c_{\text{D}}(\vec{r}) \rangle$$

Due to the proportionality of $k_{\text{B}}(\vec{r})$ to $k_{12}(\vec{r})$, the $k_{\text{B}}(\vec{r})$ space dependence is described by the 3D Gaussian beam profile $\rho_{\text{G3D}}(\vec{r})$, as reported in eq 1. Numerical solutions could be obtained for other profiles and excitation modes. However, here we are interested in deriving a general analytical dependence of the effect of the diffusion/photodynamics coupling on the average dark concentration as it can be obtained from the ACF analysis. Therefore, we search for an analytical solution in the simplest case in which the excitation volume is spherical

$$k_{\text{B}}(\vec{r}) = \begin{cases} 0 & \text{if } r = |\vec{r}| \geq L \\ \langle k_{\text{B}} \rangle & \text{if } r = |\vec{r}| < L \end{cases} \quad (12)$$

The size L must be chosen to describe the overall dispersion of the light on the excitation volume. Due to the symmetry of $k_{\text{B}}(\vec{r}) = k_{\text{B}}(|\vec{r}|) = k_{\text{B}}(r)$, we search for a spherically symmetric solution: $\langle c_{\text{D}}(\vec{r}) \rangle = \langle c_{\text{D}}(r) \rangle$. In spherical coordinates eq 11 becomes

$$\begin{aligned}D_T \frac{1}{r^2} \frac{d}{dr} \left[r^2 \frac{d}{dr} \langle c_{\text{D}}(r) \rangle \right] - k_{\text{D}} \langle c_{\text{D}}(r) \rangle + \langle k_{\text{B}} \rangle (C - \langle c_{\text{D}}(r) \rangle) &= 0 \quad \text{if } r < L \\ D_T \frac{1}{r^2} \frac{d}{dr} \left[r^2 \frac{d}{dr} \langle c_{\text{D}}(r) \rangle \right] - k_{\text{D}} \langle c_{\text{D}}(r) \rangle &= 0 \quad \text{if } r \geq L\end{aligned}\quad (13)$$

We then solve the equation for $r < L$ and $r \geq L$ and then set a continuity condition at L both for the concentration and for its derivative. This procedure, whose details can be found in the SI (“Derivation of eq 15”), leads to the radial dependence of the concentration of the molecules in the dark state, $\langle c_{\text{D}}(r) \rangle$, from which the effective dark state fraction averaged over the volume

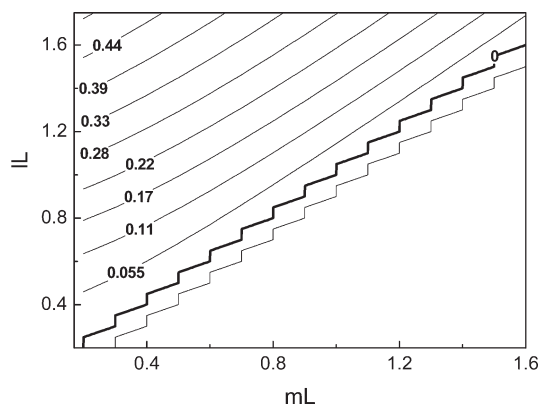


Figure 3. Contour plot of the correction factor to the dark fraction $f_{\text{dark}}^{\text{eff}}/f_{\text{dark}}^{(0)}$ in eq 15, due to the diffusion process. Values of IL and mL lower than 1 correspond to a diffusion time shorter than the dark state lifetime. Since $m \leq l$, half of the plot is null. Numbers in the plot indicate the contour levels.

can be computed as

$$f_{\text{dark}}^{\text{eff}} = \frac{\int_0^L 4\pi r^2 \langle c_D(r) \rangle dr}{\int_0^L 4\pi r^2 C dr} \quad (14)$$

eq 14 casts the dark fraction $f_{\text{dark}}^{\text{eff}}$ in terms of adimensional quantities, $IL = ((\langle k_B \rangle + k_D)L^2/D_T)^{1/2}$ and $mL = (k_D L^2/D_T)^{1/2}$. These parameters can be written in terms of the diffusion time, $\tau_{\text{diff}}^{(xy)} = (L^2/D_T)$, the decoupled dark state time, $\tau_{\text{dark}}^{(0)} = (\langle k_B \rangle + k_D)^{-1}$, and fraction, $f_{\text{dark}}^{(0)} = \langle k_B \rangle / (\langle k_B \rangle + k_D)^{-1}$, as: $IL = (\tau_{\text{diff}}^{(xy)} / \tau_{\text{dark}}^{(0)})^{1/2}$ and $mL = [(\tau_{\text{diff}}^{(xy)} / \tau_{\text{dark}}^{(0)}) (1 - f_{\text{dark}}^{(0)})]^{1/2}$. The connection between the dark fraction of molecules in the excitation volume computed with and without diffusion/photodynamics coupling is given by a composition of hyperbolic functions (see SI for details, “Derivation of eq 15”)

$$f_{\text{dark}}^{\text{eff}} = f_{\text{dark}}^{(0)} \left\{ 1 - 3 \frac{[1 + mL]}{(IL)^2} \left[\frac{(IL) \cosh(IL) - \sinh(IL)}{(mL) \sinh(IL) + (IL) \cosh(IL)} \right] \right\} \quad (15)$$

The term in the curled parentheses in eq 15 takes into account the coupling effect through the two significant variables IL and mL . The ratio $f_{\text{dark}}^{\text{eff}}/f_{\text{dark}}^{(0)}$ reported as a contour plot in Figure 3, becomes significantly less than unity for $\tau_{\text{diff}}^{(xy)}$ comparable to $\tau_{\text{dark}}^{(0)}$ whereas for $\tau_{\text{diff}}^{(xy)}/\tau_{\text{dark}}^{(0)} = (IL)^2 \gg 1$ we find $f_{\text{dark}}^{\text{eff}} \cong f_{\text{dark}}^{(0)}$.

Diffusion/Photodynamics Coupling Efficiency. To assess to what extent the predictions made on the above simplified analytical treatment of the diffusion/photodynamics coupling can be translated to the real experimental data, we need to define a parameter that quantifies the amount of diffusion/photodynamics coupling. This parameter, to be evaluated directly on the ACF decay, could then be applied to the analysis of both the experimental and the simulated data.

We expect that, in the limit of high coupling between the diffusion and the photodynamics processes, the mixing between the diffusion and the exponential time dependence of the ACF could be brought into evidence and quantified by comparing the ACF decay to that typical of diffusion induced fluctuations ($g_{\text{diff}}(t)$ in eq 4). This diffusion/photodynamics coupling efficiency parameter can be obtained by defining the G^{-1} operator

that acts on the ACF as

$$G^{-1}(g(t)) = \frac{g_0}{g(t)} - 1 \quad (16)$$

For the simple pure diffusion case (eq 4 with $f_{\text{dark}} = 0$ and $\tau_{\text{diff}}^{(z)} = \infty$) $G^{-1}(g(t))$ is given by

$$G^{-1}(g(t)) = \frac{t}{\tau_{\text{diff}}^{(xy)}} \quad (17)$$

If an additional square root term, due to the diffusion along the optical axis direction, is present in the ACF (i.e., eq 4 with $f_{\text{dark}} = 0$), then the G^{-1} function can be expanded as a function of the lag times as

$$G^{-1}(g(t)) = t \left(\frac{1}{\tau_{\text{diff}}^{(xy)}} + \frac{1}{2\tau_{\text{diff}}^{(z)}} \right) + \frac{t^2}{2} \left(\frac{1}{\tau_{\text{diff}}^{(xy)} \tau_{\text{diff}}^{(z)}} - \frac{1}{(2\tau_{\text{diff}}^{(z)})^2} \right) + o(t^2) \quad (18)$$

Since typically $\tau_{\text{diff}}^{(z)} \cong 25\tau_{\text{diff}}^{(xy)}$, the curvature of the G^{-1} function is upward.

Regarding the exponential decay that describes photodynamics contribution to the ACF in the decoupled limit, $g_{\text{PD}}(t) = 1 + (f_{\text{dark}}/(1 - f_{\text{dark}})) \exp[-t/\tau_{\text{dark}}]$, the corresponding $G^{-1}(g_{\text{PD}}(t))$ function saturates to $f_{\text{dark}}/(1 - f_{\text{dark}})$ for $\tau_{\text{dark}} \ll t$, and it would then show a downward curvature for $t \geq \tau_{\text{dark}}$, contrary to the G^{-1} of diffusion correlation functions. For small lag times, instead, the $G^{-1}(g_{\text{PD}}(t))$ function curvature can be either positive or negative, depending on the f_{dark} value ($f_{\text{dark}} < 0.5$ implies a negative curvature). In fact $G^{-1}(g_{\text{PD}}(t))$ can be expanded for $t \cong 0$ as

$$G^{-1}(g_{\text{PD}}(t)) \underset{t \rightarrow 0}{\cong} f_{\text{dark}} \frac{t}{\tau_{\text{dark}}} + \frac{f_{\text{dark}}(2f_{\text{dark}} - 1)}{2} \left(\frac{t}{\tau_{\text{dark}}} \right)^2 + o(t^2) \quad (19)$$

It is easy to verify that the G^{-1} function of the whole decoupled ACF (eq 4) increases as an exponential growth for $t \leq \tau_{\text{dark}}$ and then asymptotically becomes a straight line with a slight upward curvature for lag times larger than $\tau_{\text{diff}}^{(xy)}$. All the cases discussed above can then be described by the trial function

$$G^{-1}(g(t)) = A(1 - \exp[-t/\tau_{\text{dark}}]) + \frac{t}{\langle \tau \rangle} + \frac{t^2}{2\langle \tau \rangle^2} \sigma_2 \quad (20)$$

The exponential growth describes any fast decaying photodynamics component: the amplitude A is related to the dark fraction, f_{dark} , by $A \cong f_{\text{dark}}/(1 - f_{\text{dark}})$ (see SI, “The G^{-1} operator”). Comparison of eq 18 to eq 20 indicate that $1/\langle \tau \rangle = (1/(\tau_{\text{diff}}^{(xy)})) + (1/(2\tau_{\text{diff}}^{(z)}))$ is a measure of the effective diffusion time, and σ_2 , the curvature parameter, is expected to be slightly positive for decoupled diffusion/photodynamics fluctuations (eq 18).

This behavior is indeed found experimentally for small fluorophores, such as Rhodamine 6G, for the one-photon excitation mode, as shown in Figure 4. For the ACFs collected from Rhodamine 6G solutions (Figure 4), the best fit σ_2 is only slightly

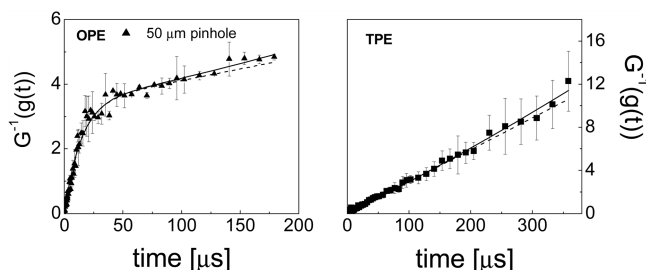


Figure 4. Analysis of the fluorescence ACF $g(t)$ in terms of the G^{-1} operator. The solid lines refer to the best fit of the data to eq 20. Panel A: One photon excitation experiment ($50\ \mu\text{m}$ confocal pinhole) on Rhodamine 6G solutions. The best fit to the trial function, $G^{-1}(g(t)) = A(1 - \exp[-t/\tau_T]) + t/\langle\tau\rangle + t^2/\langle\tau\rangle^2\sigma_2$, gives the photodynamics amplitude $A = 3.7 \pm 0.16$ and the triplet time $\tau_{\text{dark}} = 17 \pm 0.9\ \mu\text{s}$. The effective diffusion time is $\langle\tau\rangle = 140 \pm 25\ \mu\text{s}$, and the curvature parameter is $\sigma_2 = 0.14 \pm 0.07$, positive. Panel B: Two-photon excitation experiment on rhodamine 6G in ethanol. The $G^{-1}(g(t))$ function displays only a linear trend (i.e., $A \cong 0$ in eq 20) with $\langle\tau\rangle = 35 \pm 5\ \mu\text{s}$ and a slightly positive value of $\sigma_2 = 0.01 \pm 0.001$, indicating again a slight upward curvature. In both panels, the solid lines are the best fit curves. The dashed lines are the forced fit to the trial function with $\sigma_2 = 0$.

positive, indicating an upward curvature as expected for the z-diffusion component in the ACF (see eq 18). Therefore, for Rhodamine 6G, we have no indication of coupling between the photodynamics and the diffusion-induced fluctuations, as in this case the diffusion component in the ACF is well separated ($\langle\tau\rangle \cong 140\ \mu\text{s}$) from the photodynamics ($\tau_{\text{dark}} \cong 25\ \mu\text{s}$, see the OPE ACF reported in Figure 4). The two-photon (TPE) fluorescence ACF shows a substantially linear trend of $G^{-1}(g)$ and almost no photodynamics component. The $G^{-1}(g(t))$ function appears indeed fairly linear as a function of the lag time up to $\cong 4\langle\tau\rangle$, with a slight upward curvature above this lag time value.

As the photodynamics time increases, we expect that the diffusion contribution to the ACFs is no longer well separated from the photodynamics one and that the whole G^{-1} function should show a downward curvature at large lag times, reminiscence of the downward curvature of the $G^{-1}(g_{\text{PD}}(t))$ function. The curvature parameter, σ_2 , could then be taken as the signature of photodynamics fluctuations that extend over the diffusion time scale. We have proved this hypothesis on the simulated ACFs for decreasing values of k_{23} and on experimental ACFs taken on the E222Q mutant of GFPmut2, a photoswitchable protein with slow fluorescence activation times.^{4,6,36}

We discuss then in the following paragraphs the numerical simulations of FCS experiments in the limit $\tau_{\text{diff}}^{(r)} \geq \tau_{\text{dark}}^{(0)}$.

Numerical Simulation Analysis of the Diffusion/Photodynamics Coupling. We have first assessed the possibility of our coupled Monte Carlo–Brownian dynamics algorithm to reproduce correctly the short-lived triplet (dark) states. The parameters used for these simulations, reported in Table 1, correspond to a simple three-state model (only the states S_0 – S_1 – T ; see Figure 2B). In this case, there is an almost complete decoupling of the diffusion ($\tau_{\text{diff}}^{(\text{xy})} = 600\ \mu\text{s}$) and the triplet photodynamics ($\tau_{\text{dark}} = 50\ \mu\text{s}$) times due to the choice of the values of the k_{24} and k_{41} rates.

The result of the simulations of the fast dark state photodynamics, $\tau_{\text{diff}}^{(\text{xy})} \gg \tau_{\text{dark}}^{(0)}$, discussed in detail in the SI (“Numerical Simulation of the short lived dark state photodynamics”), is that

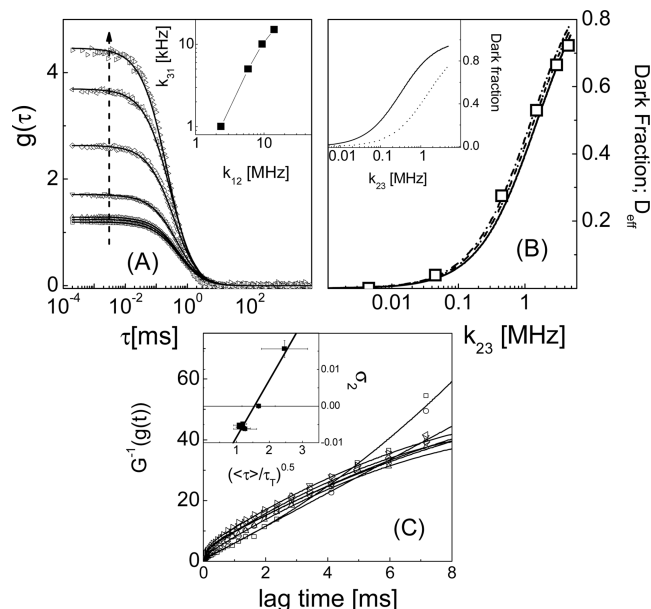


Figure 5. Simulation of the fluorescence ACFs and extrapolation of the effective dark state fraction, $f_{\text{dark}}^{\text{eff}}$. The simulation parameters are those reported in Table 1 (for the S_0 – S_1 – T part of the energy diagram in Figure 1). The dark state rates are k_{31} (assumed here 1 kHz) and k_{23} that is varied in the range $450\ \text{Hz} < k_{23} < 4.5\ \text{MHz}$. Panel A reports the simulated ACF decays corresponding to decreasing values of k_{23} , from bottom to top ($k_{23} = 0.45; 4.5; 45; 450; 1500; 3000; \text{and } 4500\ \text{kHz}$). Solid lines are the best fit of eq 4 to the simulated data. Panel B reports the effective dark state fraction $f_{\text{dark}}^{\text{eff}} = 1 - [\gamma/(\langle N \rangle g_{\text{diff}}(0))]$ derived from the best fit value of the zero lag time value of the ACF, $g_{\text{diff}}(0)$ (open squares). On the same panel we report the predictions of the triplet fraction obtained from eq 15 (by assuming $L = \omega_{xy}/2$ and one of the couples (k_{12}, k_{31}) drawn in the inset of Panel A). The line code at increasing values of k_{12} is: solid ($k_{12} = 2.35\ \text{MHz}$, $k_{31} = 1\ \text{kHz}$), dotted ($k_{12} = 5.87\ \text{MHz}$, $k_{31} = 5\ \text{kHz}$), dashed ($k_{12} = 9.4\ \text{MHz}$, $k_{31} = 10\ \text{kHz}$), and dash-dotted ($k_{12} = 14.1\ \text{MHz}$, $k_{31} = 15\ \text{kHz}$). The inset of panel B reports the trend of the dark fraction $\langle D \rangle$ (solid line; eq 15) and $f_{\text{dark}}^{(0)} = \langle k_B \rangle / (\langle k_B \rangle + k_T)^{-1}$ (dashed line) for $k_{12} = 2.35\ \text{MHz}$ and $k_{31} = 1000\ \text{Hz}$. Panel C reports the $G^{-1}(g)$ functions of the ACFs reported in Panel A (with the same symbol code) together with the best fit to eq 20 (solid lines). The value of the best fit curvature parameter σ_2 is reported as a function of the coupling parameter $(\tau_{\text{diff}}^{(\text{xy})}/\tau_T)^{1/2} \cong (\langle\tau\rangle/\tau_T)^{1/2}$, where $\langle\tau\rangle$ and τ_T are the best fit parameters obtained by the very same fitting of eq 20 to the $G^{-1}(g)$ functions.

the Monte Carlo–Brownian Dynamics algorithm correctly reproduces the diffusion and the photodynamics components of the ACFs, even in the case of excited state saturation (see eqs 7 and 8), when no coupling between these two sources of fluctuations is present.

Long Lifetime Triplet and Enhancement Photodynamics. For the numerical simulations of the PD–BD coupling, we have assumed a four-state models (S_0 – S_1 – T – D , see Figure 1), kept the S_1 – T and T – S_0 rates at the values reported in Table 1, and approached the strongly coupled case by varying the population rate of the triplet state, k_{23} , in the range $450\ \text{Hz} < k_{23} < 4.5\ \text{MHz}$ while assuming $k_{31} = 1\ \text{kHz}$. We have chosen an average excitation power of $30\ \text{mW}$ ($k_{12} \cong 2.35 \times 10^6$ excitations/s) to minimize the effect of the spatial inhomogeneity on the ACF decay (as discussed in the SI, “Effect of the beam shape on the simulated ACF”).

The ACFs obtained from the simulations can be reasonably well force fitted to a simple diffusion ACF decay ($g_{\text{diff}}(t)$ in eq 4) for all the simulated cases (Figure 5A). The best fit value of the zero lag time ACF, g_0 , can be used to measure the effective number of bright molecules in the excitation volume. In fact, the effective dark state fraction $f_{\text{dark}}^{\text{eff}}$ can be evaluated from g_0 and the input value of $\langle N \rangle$, as $f_{\text{dark}}^{\text{eff}} = 1 - [\gamma/(\langle N \rangle g_0)]$. By increasing the value of k_{23} , the effective dark fraction raises as can be seen in Figure 5A,B. Its trend can be closely reproduced (see Figure 5B) by eq 15 for the set of couples (k_{12} , k_{31}) reported as an example in the inset of Figure 5A (under the assumption $L = \omega_{xy}/2$ and $k_{12} = 2.35$ MHz and $k_{31} = 1$ kHz). It is worth noting that the values of the dark fraction that can be computed from eq 5, that assumes a complete decoupling of the PD and the diffusion dynamics, would be markedly overestimated (inset of Figure 5B) with respect to the numerical simulations and the analytical models (eq 15). Therefore, the good qualitative agreement reported in Figure 5 indicates that eq 15 correctly describes the overall effect of the diffusion/photodynamics coupling on the determination of the dark fraction from the ACFs. However, we could not measure the effective dark fraction and therefore the effective diffusion/photodynamics coupling, on real experiments, unless we knew a priori the average number of molecules $\langle N \rangle$.

This can be accomplished instead by measuring the σ_2 parameter from the analysis of the $G^{-1}(g(t))$ functions according to eq 20. The trend of $G^{-1}(g(t))$ of the simulated ACFs (Figure 5C) appears to be well described by this equation with an initial photodynamic component that is followed by a more or less linear trend. Depending on the value of k_{23} , the long lag time behavior appears to be slightly upward or downward curved, as expected by the theoretical considerations made on eq 20. The best fit values of the parameters are reported and discussed in detail in the SI ("The G^{-1} operator"). Here we focus on the curvature parameter σ_2 (see eq 20) that passes from positive (for large k_{23} values) to slightly negative values (for low values of k_{23}). If we treat the simulated ACFs as experimental data sets and estimate the coupling parameter, $IL = (\tau_{\text{diff}}^{(r)}/\tau_{\text{dark}}^{(0)})^{1/2}$, from the best fit values of $\langle \tau \rangle$ and τ_{dark} , $IL \cong (\langle \tau \rangle / \tau_{\text{dark}})^{1/2}$ (this estimate is made on the assumptions that led to eq 20; see SI for a table of the best fit parameters), we can assess that the dependence of the curvature, σ_2 , parameter, on IL , is particularly simple (Figure 5C, inset) and approximately described by a linear relationship. This result can be taken as a first indication that, despite the crude approximations that led to eq 15, the effect of the diffusion/photodynamics coupling on the ACFs scales as $IL \propto (\langle \tau \rangle / \tau_{\text{dark}})^{1/2}$, and for an implicit validation of eq 20 and of the meaning of the σ_2 parameter. From these simulation results (inset Figure 5C), we can also derive an indication of the value of the coupling parameter, $IL \cong 2$, below which the diffusion/photodynamics coupling becomes effective in the ACF decay. The analysis of the $G^{-1}(g(t))$ function could be also applied to experimental data as we will show in the next paragraphs.

It must be noted that the suggested analysis of the fluorescence fluctuations in terms of $G^{-1}(g(t))$ stands on the assumption of a robust evaluation of the ACF extrapolation to large and small lag times. At very large lag times, $g(t)$ should attain 1. However, even slight, slow changes in the concentrations due to photobleaching can result in values $g(t \rightarrow \infty) > 1$. This trend must be recognized in the ACF and, if possible, corrected or the ACF discarded from further analysis. In fact, in the presence of slow fluctuations of the fluorescence, we expect to have $B = \lim_{t \rightarrow \infty} g(t) > 1$ and that

$g(0) = B + g_0$. We can therefore write

$$G^{-1}(g_{xy}(t)) = \frac{t}{\tau_{\text{diff}}} \left(1 + \frac{B}{g_0} \left(1 + \frac{t}{\tau_{\text{diff}}} \right) \right)^{-1} \quad (21)$$

This G^{-1} function has therefore a downward curvature at large lag times since it extrapolates to B/g_0 for $t \gg \tau_{\text{diff}}$. In particular, it can be expanded as

$$G^{-1}(g(t)) = \frac{t}{\tau_{\text{diff}} \left(1 + \frac{B}{g_0} \right)} - \frac{t^2}{\tau_{\text{diff}}^2 \left(1 + \frac{B}{g_0} \right)^2} \frac{B}{g_0} + o(t^2) \quad (22)$$

The presence of the offset, B , on the ACF induces then a negative σ_2 parameter (see eq 20), $\sigma_2 \cong -2B/g_0$.

An additional source of uncertainty in the $G^{-1}(g)$ analysis is due to the need to normalize $g(t)$ and therefore to accurately evaluate $g(0)$, which is an issue for fast photodynamics of dim molecules.

Due to those considerations, it is important to assess to what extent the proposed analysis is feasible on experimental data on fluorescent proteins with slow photodynamics. To this purpose we have taken as an example the two colors photodynamics of the Mut2Q protein: Mut2Q is a photoswitchable protein endowed with millisecond activation times of the fluorescence upon double irradiation at 488 and 420 nm.⁶

Diffusion/Photodynamics Coupling in Photoswitchable Proteins: E222Q–GFPMut2. For photoswitchable proteins, beside the singlet and triplet states, at least an additional dark state must exist in which the chromophore gets trapped for relatively long times (as in Figure 1) and from which it can be freed by irradiation at higher energies with a second (probe) laser beam.

Two simple energy diagrams that describe this situation are sketched in Figure 1A,B. In the adiabatic scheme (Figure 1A), the trap state D can be depopulated by direct transition to the ground state (through k_{31}) or by pumping the chromophore from the trap state back to the singlet excited state (at the rate k_{32}) through a transition to some higher-energy state, induced by the probe beam. To the first approximation, the effect of the probe beam irradiation is that of lowering the dark state trapping propensity of the chromophore, by effectively reducing $k_{23}^{(\text{eff})} = k_{23} - \sigma_{32}I_{\text{probe}}$ (see Figure 1A). We expect that $\sigma_{23} < 0$ and $(\partial|\sigma_2|)/I_{\text{probe}} > 0$ since the diffusion/PD coupling should increase with the probe beam intensity. For the diabatic energy diagram scheme (Figure 1B), instead, the probe laser activation induces the effective increase of k_{31} as $k_{31}^{(\text{eff})} = k_{31} + \sigma_{32}I_{\text{probe}}$ (see Figure 1B) and therefore the decrease of the diffusion/PD coupling in the ACFs with I_{probe} . We expect in this case $\sigma_2 < 0$ and $(\partial|\sigma_2|)/I_{\text{probe}} < 0$.

Under growing values of the probe beam intensity, the dark fraction (D state) should decrease: this can also be derived from eq 5 by using $k_{23}^{(\text{eff})}$ instead of k_{23} or $k_{31}^{(\text{eff})}$ instead of k_{31} . On the contrary, when looking at the dark state depopulation time, τ_{dark} in eq 5, the two schemes bring an increase (Figure 1A) and a decrease (Figure 1B) of τ_{dark} and therefore of the PD–diffusion coupling.

Continuous Probe Irradiation. We first consider the case of continuous probe beam irradiation. In this kind of experiment two CW laser beams, tuned on the $S_0 \rightarrow S_1$ (pump) and the $D \rightarrow$

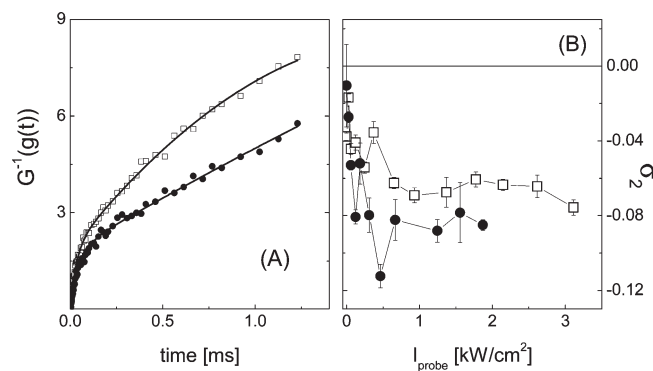


Figure 6. G^{-1} analysis of the E222Q–GFPmut2 experimental ACFs from ref 6 (Supporting Information). Panel A. Samples of $G^{-1}(g(t))$ as a function of the lag time for $I_{\text{pump}} = 17 \text{ kW/cm}^2$ and $I_{\text{probe}} = 3.7 \text{ kW/cm}^2$ (open squares) and $I_{\text{probe}} = 0.3 \text{ kW/cm}^2$ (filled circles). The solid lines are the best fit curves of eq 20 to the data with best fit parameters: $A = 1.8 \pm 0.04$, $\tau_{\text{dark}} = 48 \pm 2 \mu\text{s}$, $\langle \tau \rangle = 300 \pm 7 \mu\text{s}$, and $\sigma_2 = -0.016 \pm 0.006$ ($I_{\text{probe}} = 0.3 \text{ kW/cm}^2$); $A = 1.8 \pm 0.05$, $\tau_{\text{dark}} = 33 \pm 2 \mu\text{s}$, $\langle \tau \rangle = 280 \pm 10 \mu\text{s}$, and $\sigma_2 = -0.04 \pm 0.008$ ($I_{\text{probe}} = 3.7 \text{ kW/cm}^2$). Panel B. Summary of the analysis of the $G^{-1}(g(t))$ functions: curvature parameter, σ_2 , as a function of I_{probe} , for two values of $I_{\text{pump}} = 10 \text{ kW/cm}^2$ (filled circles) and $I_{\text{pump}} = 17 \text{ kW/cm}^2$ (open squares). The points are connected by segments to guide the eye.

D^* (probe) transitions, respectively (Figure 1A,B), are impinging on the chromophore. We apply the $G^{-1}(g)$ analysis to a series of fluorescence ACFs obtained under continuous irradiation of the pump and the probe beam as a function of their intensities reported in the Supporting Information of ref 6. The summary of this analysis is reported in Figure 6A: the G^{-1} functions show clearly the curvature effect at times larger than the dark state relaxation time (τ_{dark}) due to diffusion/photodynamics coupling.

The results reported in Figure 6B indicate that there is some coupling between diffusion and photodynamics, since $\sigma_2 < 0$, and that this coupling raises with I_{probe} . This is likely to be due to an increase of the amplitude of the relaxation component due to the action of the probe beam (in fact, measurements reported in Quercioli et al.⁶ exclude a dependence of the relaxation rate on I_{probe}). The overall decrease of the coupling at increasing values of I_{pump} , as shown in Figure 6B, is consistent with the experiments reported in Quercioli et al.⁶ and indicates that the enhancement relaxation time decreases with the increase of I_{pump} (as in Figure 4 in ref 6). These considerations suggest that the diabatic process depicted in Figure 1B is less likely to occur in Mut2Q photoswitching. It must be noted that the diabatic depopulation scheme 1B would imply a fluorescence enhancement primed by the probe beam irradiation similar to the adiabatic scheme 1A (see SI for details, “Eigenvalues of the diabatic energy diagram”) and some degree of diffusion/PD coupling at $I_{\text{probe}} = 0$. It is therefore only on the basis of the analysis of the trend of diffusion/photodynamics coupling at increasing values of the probe irradiation that we can discriminate between the two schemes.

The analytical treatment given above (eq 15) and the experimental data on the fluorescence enhancement, $\Delta F/F_0 \cong 2$,⁶ allow us also to set constraints on the rates of the transitions to and from the dark state. In fact, under dual excitation the fluorescence signal is enhanced because the dark state depopulates, and its trend can be described experimentally by the saturation

function

$$\langle F \rangle(I_{\text{pump}}, I_{\text{probe}}) = F_0(I_{\text{pump}}) + \Delta F(I_{\text{pump}}) \frac{I_{\text{probe}}}{I_{\text{probe}} + I_{\text{sat}}} \quad (23)$$

The maximum fluorescence enhancement $\Delta F/F_0$ and the saturation intensity I_{sat} could also be derived from eq 15 as a function of the k_{23} rate. Effects of transitions to higher-energy states on ΔF (see Figure 1A of ref 6) are not taken into account here for the sake of simplicity. The fluorescence enhancement can be derived by considering that, under pump beam only ($I_{\text{probe}} = 0$), the fluorescence output $\langle F \rangle(I_{\text{pump}}, 0)$ is smaller than the maximum output, $\langle F \rangle(I_{\text{pump}}, \infty) = F_0(I_{\text{pump}}) + \Delta F(I_{\text{pump}})$, due to the population of the dark state, and it can be written in terms of the dark fraction f_{dark} as $\langle F \rangle(I_{\text{pump}}, \infty)(1 - f_{\text{dark}})$. The relative enhancement factor is then

$$\frac{\Delta F(I_{\text{pump}})}{F_0(I_{\text{pump}})} = \frac{f_{\text{dark}}}{1 - f_{\text{dark}}} \quad (24)$$

We can then evaluate the possible couples (k_{23} , k_{31}) that correspond to the enhancement $\Delta F(I_{\text{pump}})/F_0(I_{\text{pump}}) \cong 2$ by setting in eq 15 $f_{\text{dark}}/(1 - f_{\text{dark}}) = 2$, as reported by Quercioli et al.⁶ To this purpose, we have also assumed, as in ref 6, $\omega_{xy} = 0.66 \mu\text{m}$, $D_T = 90 \mu\text{m}^2/\text{s}$, and $k_{12} = 580 \text{ kHz}$ or $k_{12} = 17 \text{ MHz}$ for incident pump beam powers of $\langle P \rangle = 10 \text{ mW}$ and $\langle P \rangle = 80 \text{ mW}$, respectively (Figure 7A). Figure 7A indicates that the allowed ranges of k_{23} and k_{31} span two widely different frequency ranges, Hz for k_{31} and kHz for k_{23} . The latter finding is in striking contrast with the result of the analysis of the activation process discussed by Quercioli et al.,⁶ in the limit of uncoupled diffusion/photodynamics processes: $k_{23} \cong 450 \text{ Hz}$.

We can further refine the estimate of the trapping rate k_{23} by considering also the fluorescence enhancement activation times for the photoswitching of the Mut2Q protein. These times fall in the millisecond range, $\tau \cong 1 - 10 \text{ ms}$,⁶ and can be reproduced by resorting to numerical simulations of the ACFs collected under modulated probe beam excitation.

Modulated Probe Beam Excitation. To evaluate the fluorescence activation times due to photoswitching, we have simulated the experimental ACFs while square modulating at the frequency $\nu_L = \omega/(2\pi)$ the probe beam intensity and continuously irradiating the protein with the probe beam (see Methods section). Only the adiabatic scheme 1C has been considered for this analysis. Again, we notice that the eigenvalue (relaxation rates) analysis for the two energy diagrams, 1C and 1D, provides very similar results in the limit $I_{\text{probe}} \rightarrow 0$ (see SI, “Eigenvalues of the diabatic energy diagram”). The only difference between the two schemes arises from the trend of the diffusion/photodynamics coupling at increasing I_{probe} .

The ACFs simulated under modulated probe beam irradiation were analyzed as described by Quercioli et al.⁶ Briefly, the modulation amplitude of the fluorescence emission at the frequency ν_L can be measured from $g(0, 2\pi\nu_L) = \langle \delta F^2 \rangle / \langle F \rangle^2$. This parameter decreases from the maximum value $g(0, \omega = 2\pi\nu_L \rightarrow 0) = (\Delta F^2)/(2(F_0 + F_B)^2)$ as ν_L overcomes the inverse of the fluorescence activation time (F_B is a possible background signal). If the fluorescence activation follows a double exponential growth

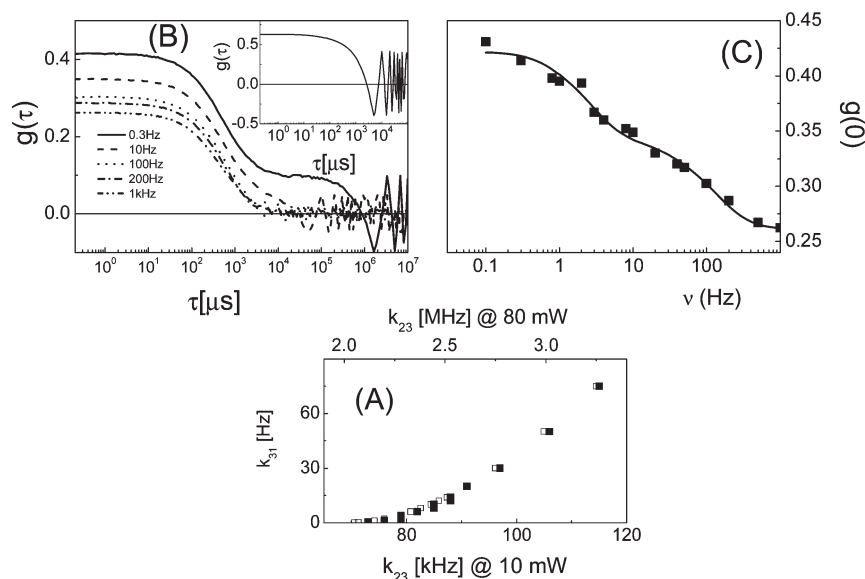


Figure 7. Panel A: couples of values of the relaxation rates k_{23} and k_{31} that satisfy the condition $f_{\text{dark}}/(1 - f_{\text{dark}}) = 2$, according to eq 15, and $\omega_{xy} = 0.66 \mu\text{m}$, $D_T = 90 \mu\text{m}^2/\text{s}$. The lower and upper scales (open and filled squares, respectively) correspond to $k_{12} = 580 \text{ kHz}$ ($\langle P \rangle = 10 \text{ mW}$) and $k_{12} = 17 \text{ MHz}$ ($\langle P \rangle = 80 \text{ mW}$). Panel B: ACFs computed on simulations run for increasing values of the probe laser modulation frequency with $I_{\text{probe}} = 1 \text{ kW}/\text{cm}^2$ and $I_{\text{pump}} = 1.7 \text{ kW}/\text{cm}^2$ and rates $k_{23} = 450 \text{ kHz}$, $k_{31} = 8 \text{ Hz}$, $k_{24} = 20\,000 \text{ Hz}$, and $k_{41} = 13\,000 \text{ Hz}$. Panel C: extrapolated $g(0, \omega)$ values obtained from panel B as a function of the modulation frequency (filled squares). The nonvanishing value of $g(0, \omega)$ for $\omega \rightarrow \infty$ is to be ascribed to a high-frequency correlation component, F_B . The solid line is the fit of the simulated data to eq 25 with best fit relaxation times $\tau_1 = 45 \text{ ms}$ and $\tau_2 = 1 \text{ ms}$.

characterized by the relaxation times τ_1 (with fraction f_1) and τ_2 (with fraction $f_2 = 1 - f_1$), the modulation ratio, $g(0, \omega)$ can be written as⁶

$$g(0, \omega = 2\pi\nu_L) = \frac{\Delta F_2}{2(F_0 + F_B)^2} \sum_{n=0,1,2} A_{2n+1}^2 \times [M_n(\omega, \tau_1, \tau_2)^2 + N_n(\omega, \tau_1, \tau_2)^2]$$

$$M_n(\omega, \tau_1, \tau_2) = f_1 L_n^R(\omega, \tau_1) + (1 - f_1) L_n^R(\omega, \tau_2)$$

$$N_n(\omega, \tau_1, \tau_2) = f_1 L_n^I(\omega, \tau_1) + (1 - f_1) L_n^I(\omega, \tau_2)$$

$$L_n^R(\omega, \tau_1) = \frac{1}{1 + (2n + 1)^2 \omega^2 \tau_1^2}$$

$$L_n^I(\omega, \tau_1) = \frac{(2n + 1) \omega \tau_1}{1 + (2n + 1)^2 \omega^2 \tau_1^2} \quad (25)$$

The coefficients, A_{2n+1} , are obtained from the Fourier expansion of the modulation square wave.⁴³

The simulations indicate indeed that the modulation of the probe beam at frequencies in the range $0.1 \text{ Hz} \leq \nu_L \leq 1 \text{ kHz}$ induce oscillations in the ACFs at times $\tau_n = n/\nu_L$, whose amplitude $g(0, 2\pi\nu_L)$ decreases as ν_L rises (see Figure 7B). Control simulations have been run to verify that the visibility of the long lag time modulations in the ACFs increases with the protein concentration (Figure 7B, inset and SI “Effect of the protein concentration on the amplitude of the modulated excitation ACF”).

The simulated $g(0, 2\pi\nu_L)$ data are reported in Figure 7C for the case $k_{12} = 576 \text{ kHz}$ ($I_{\text{pump}} = 1.7 \text{ kW}/\text{cm}^2$), $k_{23} = 450 \text{ kHz}$, and $k_{31} = 8 \text{ Hz}$ (for the simulation of the triplet state dynamics, we have assumed the rates reported in Table 1). These data closely resemble the experimental ones reported by Quercioli et al.⁶ and, when analyzed by means of eq 25, provide two relaxation times $\tau_1 \cong 1 \text{ ms}$ and $\tau_2 \cong 48 \text{ ms}$, very close to the experimental best fit relaxation times $\tau_1 = 1.3 \pm 0.2 \text{ ms}$ and $\tau_2 = 33 \pm 5 \text{ ms}$ found by Quercioli et al.⁶

We have not made here a direct fit of the simulated ACFs to the experimental data. However, we notice that qualitative (Figure 7B) and quantitative (Figure 7C) agreement clearly confirms the validity of the simulation model (within scheme 1A) and the values of the relaxation rates, $k_{23} \cong 450 \text{ kHz}$ and $k_{31} \cong 10 \text{ Hz}$, for the Mut2Q protein. The substantially higher value of k_{23} with respect to the previously experimentally determined one,⁶ $k_{\text{isc}} = k_{23} \cong 400 \text{ Hz}$, is then to be ascribed to the coupling between the diffusion and the PD processes, thereby showing again the relevance of this phenomenon for the FCS data analysis in these specific cases. Finally, we again point out that a demodulation spectrum as that reported in Figure 7C could have been obtained also within the framework of scheme 1B (adiabatic transition), though with lower rates ($k_{23} \cong 40\text{--}50 \text{ kHz}$). However, in this case, as discussed previously, the PD–diffusion coupling should decrease with increasing probe intensities, opposite to the experimental behavior reported in Figure 6.

CONCLUSIONS

We have analyzed the effect of the coupling between the molecular Brownian diffusion (BD) and the chromophore photodynamics (PD) on the shape of the fluorescence autocorrelation functions. For the case of uniform spherically symmetric excitation volume, the chromophore dark fraction scales, with respect to the uncoupled result, as the square root of the ratio of the diffusion to the photodynamics relaxation times, $IL = ((\tau_{\text{diff}}^{(xy)})/\tau_{\text{dark}})^{1/2}$. We have also discussed a graphical method, called here G^{-1} analysis, for the evaluation of the BD–PD coupling on the fluorescence ACFs. This kind of analysis is based on the evaluation of the sign of the large lag times curvature (σ_2) of the inverse of the ACF and has provided us with an estimate of the limit of the coupling parameter, $IL \cong 2$, below which the effect of the BD–PD coupling on the ACF decay becomes effective.

The G^{-1} analysis has been validated on numerical simulations and applied to data on the photoswitchable protein Mut2Q. On the numerical simulation, we find that the curvature parameter, σ_2 , scales with the ratio $((\tau_{\text{diff}}^{xy})/\tau_{\text{dark}})^{1/2}$. This result indicates that, despite the crudeness of the approximations made here, our simple analytical treatment describes qualitatively rather well the dark fraction values and the ACF shape and suggests a data analysis method to be applied to the experimental ACFs to evaluate the amount of diffusion/PD coupling.

Finally, we show how numerical simulations applied to the study of the GFP slow photoswitching dynamics are essential to correctly estimate the relaxation rates of the process. For the case of the photoswitchable Mut2Q protein, the estimate of the excited singlet to the dark state relaxation, k_{23} , is approximately 3 orders of magnitude lower when we do not take into account the diffusion–photodynamics coupling.

■ ASSOCIATED CONTENT

S Supporting Information. Details of the derivation of eq 10, the derivation of the fraction of the dark molecules in the excitation volume (eq 15), the effect of the beam shape on the simulated ACFs for the OPE and TPE cases, the definition and use of the $G^{-1}(g(t))$ operator, and the analysis of the eigenvalues (for $I_{\text{probe}} = 0$) of the diabatic energy scheme. This material is available free of charge via the Internet at <http://pubs.acs.org>.

■ AUTHOR INFORMATION

Corresponding Author

*E-mail: giuseppe.chirico@mib.infn.it.

■ ACKNOWLEDGMENT

The authors wish to thank prof. Francesco Montalenti for his valuable advice on the numerical simulations. This work has been also funded by the PRIN MIUR fund 2008 to M.C. (2008JZ4MLB) and by the FP7 program ENCITE (contract n. 201842).

■ REFERENCES

- (1) Magde, D.; Elson, E.; Webb, W. W. *Phys. Rev. Lett.* **1972**, *29*, 705.
- (2) Chen, Y.; Müller, J. D.; So, P.; Gratton, E. *Biophys. J.* **1999**, *77*, 553.
- (3) Chirico, G.; Olivini, F.; Beretta, S. *Appl. Spectrosc.* **2000**, *54*, 1084.
- (4) Jung, J.; Brauchle, C.; Zumbusch, A. *J. Chem. Phys.* **2001**, *114*, 3149.
- (5) Bosisio, C.; Quercioli, V.; Collini, M.; D'Alfonso, L.; Baldini, G.; Bettati, S.; Campanini, B.; Raboni, S.; Chirico, G. *J. Phys. Chem. B* **2008**, *112*, 8806.
- (6) Quercioli, V.; Bosisio, C.; Daglio, S. C.; Rocca, F.; D'Alfonso, L.; Collini, M.; Baldini, G.; Chirico, G.; Bettati, S.; Raboni, S.; Campanini, B. *J. Phys. Chem. B* **2010**, *114*, 4664.
- (7) Schwille, P.; Korlach, J.; Webb, W. W. *Cytometry* **1999**, *36*, 176.
- (8) Haustein, E.; Schwille, P. *Curr. Opin. Struct. Biol.* **2004**, *14*, 531.
- (9) Kim, S. A.; Heinze, K. G.; Schwille, P. *Nat. Methods* **2007**, *4*, 963.
- (10) Day, R. N.; Davidson, M. W. *Chem. Soc. Rev.* **2009**, *38*, 2887.
- (11) Bizzarri, R.; Serresi, M.; Luin, S.; Beltram, F. *Anal. Bioanal. Chem.* **2009**, *393*, 1107.
- (12) Magde, D.; Webb, W. W.; Elson, E. L. *Biopolymers* **1974**, *13*, 29.
- (13) Schwille, P.; Haupts, U.; Maiti, S.; Webb, W. W. *Biophys. J.* **1999**, *77*, 2251.
- (14) Dittrich, P. S.; Schwille, P. *Appl. Phys. B: Laser Opt.* **2001**, *73*, 829.
- (15) Schwille, P. *Cell Biochem. Biophys.* **2001**, *34*, 382.
- (16) Haupts, U.; Maiti, S.; Schwille, P.; Webb, W. W. *Proc. Natl. Acad. Sci. U.S.A.* **1998**, *95*, 13573.
- (17) Widengren, J.; Terry, B.; Rigler, R. *Chem. Phys.* **1999**, *249*, 259.
- (18) Jung, G.; Mais, S.; Zumbusch, A.; Bräuchle, C. *J. Phys. Chem. A* **2000**, *104*, 873.
- (19) Chen, Y.; Müller, J. D.; Ruan, Q. Q.; Gratton, E. *Biophys. J.* **2002**, *82*, 133.
- (20) Hess, S. T.; Heikal, A. A.; Webb, W. W. *J. Phys. Chem. B* **2004**, *108*, 10138.
- (21) Veettil, S.; Budisa, N.; Jung, G. *Biophys. Chem.* **2008**, *136*, 38.
- (22) Elson, E. L.; Magde, D. *Biopolymers* **1974**, *13*, 1.
- (23) Enderlein, J.; Gregor, I.; Patra, D.; Dertinger, T.; Kaupp, U. B. *ChemPhysChem* **2005**, *6*, 2324.
- (24) Gregor, I.; Patra, D.; Enderlein, J. *ChemPhysChem* **2005**, *6*, 164.
- (25) Petrášek, Z.; Schwille, P. *Biophys. J.* **2008**, *94*, 1437.
- (26) Andresen, M.; Stiel, A. C.; Foelling, J.; Wenzel, D.; Schoenle, A.; Egner, A.; Eggeling, C.; Hell, S. W.; Jakobs, S. *Nat. Biotechnol.* **2008**, *26*, 1035.
- (27) Hell, S. *Nat. Biotechnol.* **2003**, *21*, 1347.
- (28) Widengren, J.; Mets, U.; Rigler, R. *Chem. Phys.* **1999**, *250*, 171.
- (29) Bizzarri, R.; Nifosì, R.; Abbruzzetti, S.; Rocchia, W.; Guidi, S.; Arosio, D.; Garau, G.; Campanini, B.; Grandi, E.; Ricci, F.; Viappiani, C.; Beltram, F. *Biochemistry* **2007**, *46*, 5494.
- (30) Ando, T.; Meguro, T.; Yamato, I. *Mol. Simul.* **2003**, *29*, 471.
- (31) Ermak, D. L.; McCammon, J. A. *Phys. Rev. Lett.* **1978**, *69*, 1352.
- (32) Chirico, G.; Langowski, J. *Macromolecules* **1992**, *25*, 769.
- (33) Doi, M.; Edwards, S. F. *The Theory of Polymer Dynamics*; Clarendon Press: Oxford, UK, 1986; pp 46–89.
- (34) Gillespie, D. J. *Comput. Phys.* **1976**, *22*, 403.
- (35) Bizzarri, R.; Serresi, M.; Cardarelli, F.; Abbruzzetti, S.; Campanini, B.; Viappiani, C.; Beltram, F. *J. Am. Chem. Soc.* **2010**, *132*, 85.
- (36) Jung, G.; Wiehler, J.; Zumbusch, A. *Biophys. J.* **2005**, *88*, 1932.
- (37) Albota, M. A.; Xu, C.; Webb, W. W. *Appl. Opt.* **1998**, *37*, 7352.
- (38) Blab, G. A.; Lommerse, P. H. M.; Cognet, L.; Harms, G. S.; Schmidt, T. *Chem. Phys. Lett.* **2001**, *350*, 71.
- (39) Mertz, J. *Eur. Phys. J. D* **1998**, *3*, 53.
- (40) Eggeling, C.; Widengren, J.; Brand, L.; Schaffer, J.; Felekyan, S.; Seidel, C. A. M. *J. Phys. Chem. A* **2006**, *110*, 2979.
- (41) Petrášek, Z.; Schwille, P. *ChemPhysChem* **2008**, *9*, 147.
- (42) Widengren, J.; Mets, U.; Rigler, R. *J. Chem. Phys. B* **1995**, *99*, 13368.
- (43) Sneddon, I. N. *Fourier Transform*; Dover Inc.: New York, USA, 1995.